mQSM: Multitask Learning-based Quantitative Susceptibility Mapping for Iron Analysis in Brain

Junjie He[1,2], Bangkang Fu[2], Zhenliang Xiong[1,2], Yunsong Peng[2], and Rongpin Wang[2,*]

[1] Key Laboratory of Intelligent Medical Image Analysis and Precise Diagnosis of Guizhou Province, College of Computer Science and Technology, Guizhou University, No. 2708, Huaxi Avenue, Guiyang, 550025, Guizhou, China
[2] Department of Radiology, Guizhou Provincial People's Hospital, No. 83, Zhongshan Dong Road, Guiyang, 550002, Guizhou, China
*Corresponding author: wangrongpin@126.com

Abstract. Quantitative analysis of brain iron is widely utilized in neurodegenerative diseases, typically accomplished through the utilization of quantitative susceptibility mapping (QSM) and medical image registration. However, this approach heavily relies on registration accuracy, and image registration can alter QSM values, leading to distorted quantitative analysis results. This paper proposes a multi-modal multitask QSM reconstruction algorithm (mQSM) and introduces a mutual Transformer mechanism (mTrans) to efficiently fuse multi-modal information for QSM reconstruction and brain region segmentation tasks. mTrans leverages Transformer computations on ***Q***uery and ***V***alue feature matrices for mutual attention calculation, eliminating the need for additional computational modules and ensuring high efficiency in multi-modal data fusion. Experimental results demonstrate an average dice coefficient of 0.92 for segmentation, and QSM reconstruction achieves an SSIM evaluation of 0.9854 compared to the gold standard. Moreover, segmentation-based (mQSM) brain iron quantitative analysis shows no significant difference from the ground truth, whereas the registration-based approach exhibits notable differences in brain cortical regions compared to the ground truth. Our code is available at https://github.com/TyrionJ/mQSM.

Keywords: Quantitative susceptibility mapping · Brain region segmentation · Brain iron analysis · Deep learning.

1 Introduction

Quantitative susceptibility mapping (QSM) is an MRI technique utilized for the quantification of spatial magnetic susceptibility distribution [6]. QSM has been widely applied in the auxiliary diagnosis of neurodegenerative diseases such as Alzheimer's disease [3,4], Parkinson's disease [24], multiple sclerosis [18], Huntington's disease [22], etc. Currently, the clinical utilization of quantitative analysis for QSM is limited to manual regions of interest (ROI) selection and measuring susceptibility values for diagnosing iron deposition [16]. However, manual

ROI selection lacks objectivity and may not fully capture comprehensive changes in iron homeostasis across various brain regions. Besides, in the process of reconstructing QSM, dipole inversion is essential for computing QSM from a field map, which involves dividing the field by the dipole kernel in the Fourier domain and makes the dipole inversion an ill-conditioned division problem [8].

To solve these problems, the current approach involves initial QSM reconstruction followed by a comprehensive analysis of global brain iron homeostasis changes using medical image registration. There are primarily two categories of QSM reconstruction algorithms: traditional methods represented by COSMOS [11], TKD [17], iLSQR [10], and STAR-QSM [21], and deep learning approaches such as QSMNet [23], AdaIN-QSM [14], and msQSM [7]. AdaIN-QSM and msQSM, in particular, utilize single-direction data to achieve QSM reconstruction at any resolution, approaching the gold standard COSMOS, which requires data acquisition in at least three directions. For medical image registration, commonly used traditional methods include FLIRT [5], NiftyReg [13], and ANTs [1]. Some emerging deep learning methods, such as TransMorph [2] and MD-SGT [19], have also shown remarkable performance in registration. Although these registration methods achieve accurate results for subcortical structures, the precision for certain cortical regions falls short of the requirements for quantitative iron homeostasis analysis. Furthermore, the registration process not only alters numerical values in QSM, distorting results but also leads to the loss of morphological information.

To address the above issues. We propose a mutual transformer network (mTrans-Net) to integrate multi-modal information and accomplish multitask QSM reconstruction. The main contributions of this study are as follows:

1) We propose a lightweight and efficient multi-modal data fusion mechanism named mutual Transformer (mTrans);
2) We propose a precise all-in-one solution for QSM reconstruction and brain iron analysis;
3) The proposed mTrans can be applied to other Transformer-based multimodal fusion models, significantly boosting their performance.

2 Method

The framework of the mTrans-Net method is presented in Fig.1, which primarily consists of two sub-networks: the reconstruction network and the fusion segmentation network. The reconstruction network consists of 6 ResBlocks and is trained in a self-supervised manner. The segmentation model, based on UNet, incorporates a mutual Transformer mechanism to fuse QSM and T1 data, leveraging the advantages of QSM for clear presentation of brain nuclei and T1 for clear presentation of the cortex, to accomplish brain region segmentation tasks.

2.1 QSM theory

QSM reconstruction When subjected to an external main magnetic field, tissues undergo magnetization, leading to the induction of magnetic perturbations

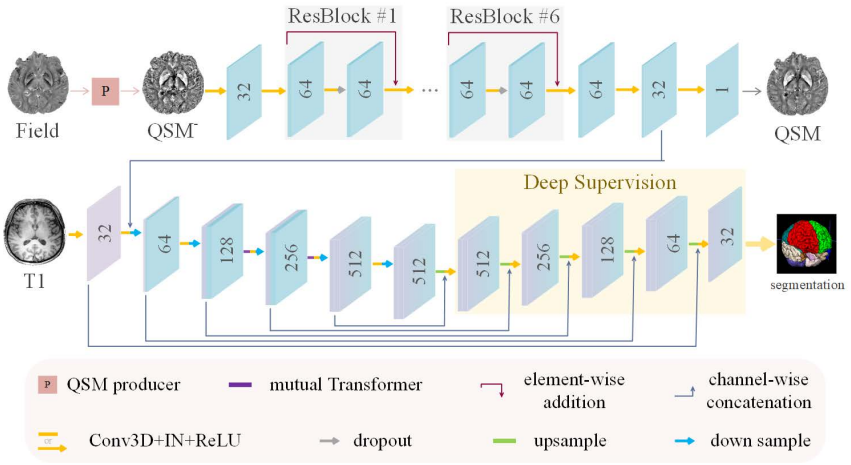

Fig. 1. The architecture of the multi-task QSM reconstruction network. The numbers represent the feature channels. IN: instance norm 3D, ReLU: leakyReLU.

along the field. As demonstrated by the media effect Lorentz correction and the Maxwell magnetostatic equations [12], the perturbation adheres to

$$\delta_B(\boldsymbol{r}) = \frac{3\cos^2\alpha - 1}{4\pi|\boldsymbol{r}|^3} \otimes \chi(\boldsymbol{r}), \tag{1}$$

where $\delta_B(\boldsymbol{r}) = [B(\boldsymbol{r}) - B_0]/B_0$ represents the perturbation, with B indicating the local magnetic field map. Here, $\boldsymbol{r}$, α, and $\otimes$ denote the spatial coordinate, the angle between vector $\boldsymbol{r}$ and the main field, and the 3D convolution operator, respectively. χ represents the QSM to be solved.

Utilizing a dipole kernel, the equation above can be simplified as a pointwise multiplication in the Fourier domain [15]:

$$\Delta_B(\boldsymbol{k}) = \left(\frac{1}{3} - \frac{k_p^2}{k^2}\right) \cdot X(\boldsymbol{k}) = D(\boldsymbol{k}) \cdot X(\boldsymbol{k}), \tag{2}$$

where Δ_B and X are the Fourier transforms of δ_B and χ, respectively. k is the magnitude of $\boldsymbol{k}$ in the k-space. $D(\boldsymbol{k})$ is the resolution-dependent dipole kernel and k_p is the projection of $\boldsymbol{k}$ onto the main field. QSM reconstruction solves the ill-posed problem Eq. 2 to obtain X based on B.

QSM producer We propose an initial QSM reconstruction algorithm based on edge detection, utilizing the TKD method to decouple the dependence of resolution and orientation producing a raw QSM result (QSM^-):

$$\begin{cases} \text{QSM}^- = \mathcal{S}_{\Delta_B} * \text{TKD}_{0.1} + (1 - \mathcal{S}_{\Delta_B}) * \text{TKD}_{0.2} \\ \text{TKD}_{thr}(\boldsymbol{k}) = \frac{\text{sign}(D(\boldsymbol{k}))}{\max(|D(\boldsymbol{k})|, thr)} \cdot \Delta_B(\boldsymbol{k}) \end{cases}, \tag{3}$$

where $\mathcal{S}_{\Delta_B}$ is the normalized result of the Sobel operator applied to Δ_B and thr is the threshold used in the TKD method to balance precision and artifacts. $\mathcal{S}$ offers an approximation of the boundary delineation between neighboring tissues, while $(1-\mathcal{S})$ quantifies the extent of field fluctuation within a tissue.

2.2 Mutual Transformer

The proposed mutual Transformer (mTrans) is based on the self-attention mechanism [20], which performs computation using three feature tensors–Q, K, and V: $SA = softmax(\frac{QK^T}{S})V$. The proposed mTrans utilizes Q and V features from dual modalities for feature fusion:

$$\begin{cases} \mathrm{MA} = Q_1 \cdot Q_2^T \\ \\ \mathrm{mTrans} = cat([SA_1, \mathrm{MA} \cdot V_2, SA_2, \mathrm{MA} \cdot V_1]) \end{cases}, \tag{4}$$

where Q_1 and Q_2 are used to compute mutual attention (MA) and $\mathrm{MA} \cdot V_i$ represents the i-th mutual feature. Finally, concatenate the self-attention features and mutual features to complete the mTrans fusion.

2.3 Loss function

The QSM reconstruction subnetwork was trained in a self-supervised manner:

$$\begin{cases} \mathcal{L}_C = \left\| \mathrm{abs}\left(\mathrm{QSM}^-\right)\left(\mathrm{QSM}^- - \mathrm{QSM}\right) \right\|_1 \\ \\ \mathcal{L}_M = \left\| \mathcal{S}_{\Delta_B} - \mathcal{S}_{QSM} \right\|_1 \end{cases}, \tag{5}$$

where $\mathcal{L}_C$ is the consistency loss and $\mathcal{L}_M$ is the morphological loss based on the Sobel operator on Δ_B and QSM. Set the reconstruction loss $\mathcal{L}_{rec} = \mathcal{L}_C + 0.01\mathcal{L}_M$.

The segmentation employs dice and cross-entropy for deep supervision:

$$\begin{cases} \mathcal{L}_{dice}\left(p,q\right) = -\frac{2\times\sum_{i=1}^{n} p_i \cdot q_i}{\sum_{i=1}^{n} p_i + \sum_{i=1}^{n} q_i} \\ \\ \mathcal{L}_{CE}\left(p,q\right) = -\frac{1}{n}\sum_{i=1}^{n} q_i \mathrm{log} p_i + (1-q_i)\mathrm{log}(1-p_i) \end{cases}, \tag{6}$$

where n is the voxel number of the input data, $p_i \in [0,1]$ denotes the prediction probability, and $q_i \in \{0,1\}$ signifies the ground truth. Combine the two loss $\mathcal{L} = \mathcal{L}_{dice} + \mathcal{L}_{CE}$ and set $\mathcal{L}_{seg} = \sum_{i=1}^{5} \frac{\mathcal{L}_i}{2^{i-1}}$ as segmentation loss where $\mathcal{L}_i$ is the $\mathcal{L}$ of the i-th layer (from the shallow to deep).

Finally, set $\mathcal{L}_T = \mathcal{L}_{rec} + \mathcal{L}_{seg}$ as the overall training loss of the network.

3 Experiments

3.1 Dataset and Experimental Settings

The proposed mQSM was trained on an in-house dataset acquired from 45 subjects with QSM and aligned T1 data using a 3T GE scanner. The acquisition parameters for QSM were: resolution = $1\times1\times1$ mm^3, FOV = $256\times256\times136$ mm^3,

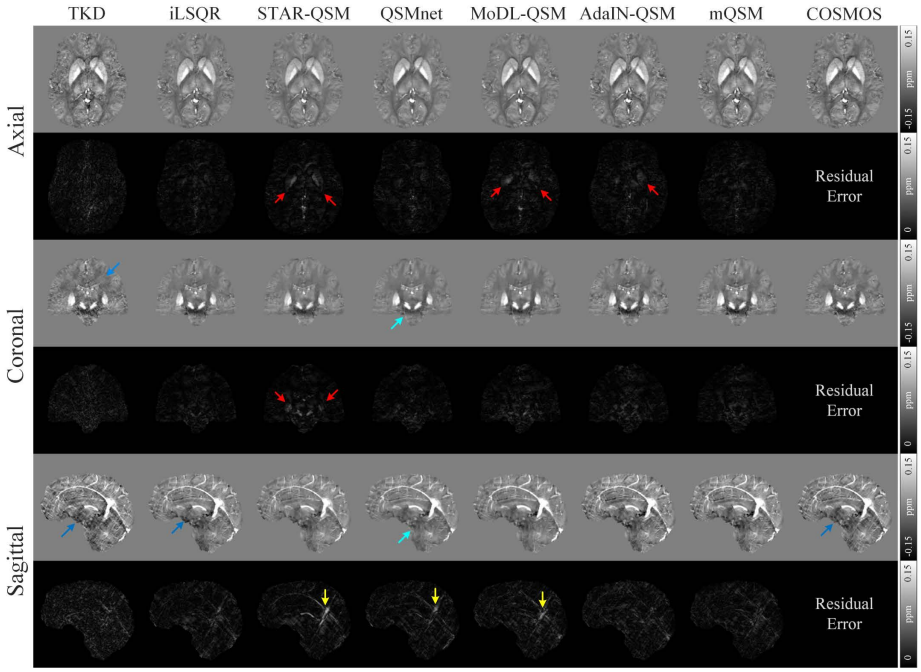

Fig. 2. Three orthogonal perspectives of QSM reconstruction results, including residual errors relative to COSMOS, are depicted.

TR = 41.81 ms, $TE_1/\Delta TE$ = 3.27/2.35 ms, and 16 echoes. The acquisition parameters for T1 were: resolution = $1 \times 1 \times 1$ mm^3, TR = 8.46 ms, flip angle = 15°, and TE = 3.25 ms. The segmentation labels, comprising 36 brain regions, were obtained by imaging professionals with the assistance of MONAI Label AI.

In assessing the QSM reconstruction performance, we chose the dataset from the 2016 QSM challenge [9] as it allows reconstruction into the established gold standard, COSMOS. The dataset was obtained from a healthy volunteer using a 3T Siemens Scanner, employing 12 sampling orientations.

The assessment encompassed various methods, with a truncation threshold of 0.2 applied to TKD. COSMOS calculations were performed using four orientation samplings. The reconstructed QSM outcomes were averaged across the respective four orientation samplings. QSMnet and MoDL-QSM underwent retraining based on pre-existing models. Additionally, AdaIN-QSM was trained using multi-resolution data.

To assess the disparity between brain iron quantification based on brain region segmentation and that based on medical image registration, we employed several classic registration methods such as FLIRT, NiftyReg, and ANTs.

3.2 Reconstruction evaluation

Although mQSM is trained using field maps and T1 multimodal data, the reconstruction network does not involve T1 data. Consequently, the model supports QSM reconstruction solely based on the input field maps.

Qualitative evaluation Fig. 2 displays the reconstruction outcomes using various methods across three orthogonal planes, alongside residual error maps. TKD results exhibit noticeable noise and streaking artifacts (indicated by blue arrows). Conversely, iLSQR, AdaIN-QSM, and mQSM exhibit reduced errors compared to COSMOS, although artifacts are evident in the sagittal view of iLSQR and COSMOS (blue arrows). STAR-QSM and MoDL-QSM produce smoother reconstructions but display larger errors in specific brain regions, such as the lenticular nucleus (red arrows), inferior sagittal sinus, and internal cerebral vein (yellow arrows). In summary, AdaIN-QSM and mQSM yield visually superior outcomes with lower residual errors compared to COSMOS, demonstrating the capability to mitigate streaking artifacts.

Table 1. Comparison of quantitative performance metrics for QSM reconstruction methods relative to COSMOS, based on data from the 2016 QSM Challenge.

Methods	SSIM	PSNR(dB)	NRMSE	HFEN
TKD	0.9686	40.13	0.4354	46.25
iLSQR	0.9836	42.51	0.3840	**32.49**
STAR-QSM	**0.9857**	42.14	0.4561	36.25
QSMnet	0.9763	42.80	0.4085	32.67
MoDL-QSM	0.9551	42.56	0.4133	36.87
AdaIN-QSM	0.9840	42.44	0.3644	34.89
mQSM	0.9854	**42.99**	**0.3315**	32.99

Bold values indicate the best metrics.

Quantitative evaluation Table 1 presents the quantitative outcomes of the proposed mQSM alongside other methods, assessed through structural similarity index (SSIM), peak signal-to-noise ratio (PSNR), normalized root mean square error (NRMSE), and high-frequency error norm (HFEN). Among all methods, iLSQR exhibits the lowest HFEN (32.49). QSMnet shows relatively higher PSNR (42.80) and lower HFEN (32.67). mQSM achieves the highest SSIM (0.9854), PSNR (42.99 dB), and lowest NRMSE (0.3315), with only a marginal increase in HFEN by 1.54% compared to the optimal metrics.

3.3 Brain iron analysis

The currently prevalent methods for whole-brain iron quantification analysis rely on registration. This section demonstrates the discrepancies between brain iron

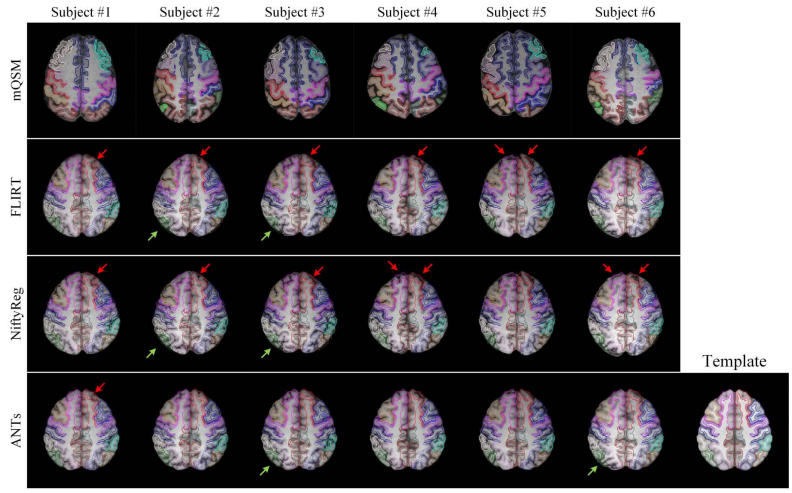

Fig. 3. The comparison figure displays the segmentation results of mQSM and different registration methods on brain regions. Colored polygons delineate the cortical areas.

quantification analyses based on brain segmentation and registration. Here, registration employs the Montreal Neurological Institute (MNI) standard brain template, where registration is initially performed on T1 images and subsequently applied to the deformation field on QSM images.

Qualitative evaluation Fig. 3 displays the brain segmentation results obtained using the proposed mQSM and the matching results of the standard brain template using three commonly employed registration methods. The mQSM achieves precise segmentation results for the brain cortex, whereas registration methods exhibit significant discrepancies in matching brain areas such as the frontal lobe (red arrows) and parietal lobe (green arrows) with the brain template.

Table 2. The discrepancy in brain iron quantitative analysis (mean ± std in ppb) between mQSM segmentation and registration methods.

Region	Ground truth	mQSM	FLIRT	NiftyReg	ANTs
frontal lobe (L)	4.6±0.4	4.7±0.5	⋆⋆2.8±0.3	⋆⋆2.9±0.3	⋆⋆3.2±0.2
lateral temporal (R)	-2.4±0.5	-2.5±0.5	⋆⋆-0.9±0.4	⋆⋆-0.9±0.4	⋆⋆-0.7±0.3
medial temporal (R)	-2.2±0.7	-2.1±0.7	-1.5±0.7	-1.3±0.8	⋆-0.2±0.7
caudate (R)	30.7±2.4	31.8±2.4	29.7±2.5	31.6±2.5	32.1±2.3
pallidum (R)	81.1±3.7	82.5±3.7	76.5±6.4	⋆71.1±6.2	78.8±4.9
thalamus (R)	-1.1±1.2	-1.1±1.2	-2.1±0.9	⋆-2.8±0.9	-1.4±0.8
accumbens area (R)	-33.3±3.5	-33.4±3.4	⋆⋆-8.3±5.3	⋆⋆-13.4±4.8	⋆-24.2±4.3

⋆⋆: $p \leq 0.01$ and ⋆: $0.01 < p \leq 0.05$ reference to the ground truth.

Quantitative evaluation Table 2 illustrates the differences in iron quantitative analysis of randomly selected 7 brain regions (All can be found in the supplementary materials) among the 36 brain areas between segmentation and registration methods. The QSM used is the mQSM reconstruction result, and the ground truth is the average magnetization value of brain regions calculated based on segmentation labels. The table demonstrates that mQSM brain iron quantification aligns closely with the ground truth, with no notable differences. In contrast, the registration-based method shows significant variances primarily in cortical analysis, with no significant differences in nucleus analysis.

Table 3. The mQSM results integrated with different segmentation models. mQSM_* denotes the use of * as the segmentation module.

Methods	dice	recall	precision	HD95	ASD
$\text{mQSM}_{\text{U-Net}}$	0.86	0.83	0.89	2.17	1.08
$\text{mQSM}_{\text{U-Net}}$	0.86	0.83	0.89	2.17	1.08
$\text{mQSM}_{\text{U-Net}}$	0.86	0.83	0.89	2.17	1.08
mQSM	0.86	0.83	0.89	2.17	1.08

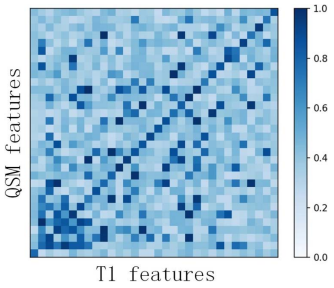

Fig. 4. Mutual attention map.

As the mTrans is exclusively employed in the segmentation task, ablation experiments were conducted solely on the segmentation module to verify the effectiveness. Table 3 indicates that mQSM (U-Net+SA+MA) achieves the best segmentation results compared to U-Net+SA as the segmentation network. Fig. 4 shows the normalized mutual attention (MA) matrix, which is generally symmetric, indicating significant correlations between certain multimodal features.

4 Conclusion

This study introduces a multitask QSM reconstruction algorithm for comprehensive brain iron distribution analysis. Unlike conventional methods relying on reconstructed images and template registration, our approach avoids registration-induced QSM value changes. Experimental results show that mQSM yields comparable iron quantification across brain regions to the gold standard. Moreover, we propose a mutual Transformer mechanism for multimodal fusion, enhancing fusion efficacy and segmentation accuracy.

Acknowledgments. This study was funded by the Guizhou Senior Innovative Talent Project [QKHPTRC-GCC [2022]041-1].

Disclosure of Interests. The authors have no competing interests to declare that are relevant to the content of this article.

References

1. Avants, B.B., Tustison, N.J., Song, G., Cook, P.A., Klein, A., Gee, J.C.: A reproducible evaluation of ants similarity metric performance in brain image registration. NeuroImage **54**, 2033–2044 (2 2011). https://doi.org/10.1016/j.neuroimage.2010.09.025
2. Chen, J., Frey, E.C., He, Y., Segars, W.P., Li, Y., Du, Y.: Transmorph: Transformer for unsupervised medical image registration. Medical Image Analysis **82**, 102615 (11 2022). https://doi.org/10.1016/j.media.2022.102615
3. Chen, L., Soldan, A., Oishi, K., Faria, A., Zhu, Y., Albert, M., van Zijl, P.C.M., Li, X.: Quantitative susceptibility mapping of brain iron and -amyloid in mri and pet relating to cognitive performance in cognitively normal older adults. Radiology **298**, 353–362 (2 2021). https://doi.org/10.1148/radiol.2020201603
4. Cogswell, P.M., Wiste, H.J., Senjem, M.L., Gunter, J.L., Weigand, S.D., Schwarz, C.G., Arani, A., Therneau, T.M., Lowe, V.J., Knopman, D.S., Botha, H., Graff-Radford, J., Jones, D.T., Kantarci, K., Vemuri, P., Boeve, B.F., Mielke, M.M., Petersen, R.C., Jack, C.R.: Associations of quantitative susceptibility mapping with alzheimer's disease clinical and imaging markers. NeuroImage **224**, 117433 (1 2021). https://doi.org/10.1016/j.neuroimage.2020.117433
5. Greve, D.N., Fischl, B.: Accurate and robust brain image alignment using boundary-based registration. NeuroImage **48**, 63–72 (10 2009). https://doi.org/10.1016/j.neuroimage.2009.06.060
6. Haacke, E.M., Liu, S., Buch, S., Zheng, W., Wu, D., Ye, Y.: Quantitative susceptibility mapping: current status and future directions. Magnetic Resonance Imaging **33**, 1–25 (1 2015). https://doi.org/10.1016/j.mri.2014.09.004
7. He, J., Peng, Y., Fu, B., Zhu, Y., Wang, L., Wang, R.: msqsm: Morphology-based self-supervised deep learning for quantitative susceptibility mapping. NeuroImage **275**, 120181 (7 2023). https://doi.org/10.1016/j.neuroimage.2023.120181
8. Kee, Y., Liu, Z., Zhou, L., Dimov, A., Cho, J., de Rochefort, L., Seo, J.K., Wang, Y.: Quantitative susceptibility mapping (qsm) algorithms: Mathematical rationale and computational implementations. IEEE Transactions on Biomedical Engineering **64**, 2531–2545 (11 2017). https://doi.org/10.1109/TBME.2017.2749298
9. Langkammer, C., Schweser, F., Shmueli, K., Kames, C., Li, X., Guo, L., Milovic, C., Kim, J., Wei, H., Bredies, K., Buch, S., Guo, Y., Liu, Z., Meineke, J., Rauscher, A., Marques, J.P., Bilgic, B.: Quantitative susceptibility mapping: Report from the 2016 reconstruction challenge. Magnetic Resonance in Medicine **79**, 1661–1673 (3 2018). https://doi.org/10.1002/mrm.26830
10. Li, W., Wang, N., Yu, F., Han, H., Cao, W., Romero, R., Tantiwongkosi, B., Duong, T.Q., Liu, C.: A method for estimating and removing streaking artifacts in quantitative susceptibility mapping. NeuroImage **108**, 111–122 (3 2015). https://doi.org/10.1016/j.neuroimage.2014.12.043, iLSQR
11. Liu, T., Spincemaille, P., de Rochefort, L., Kressler, B., Wang, Y.: Calculation of susceptibility through multiple orientation sampling (cosmos): A method for conditioning the inverse problem from measured magnetic field map to susceptibility source image in mri. Magnetic Resonance in Medicine **61**, 196–204 (1 2009). https://doi.org/10.1002/mrm.21828, cOSMOS
12. Marques, J., Bowtell, R.: Application of a fourier-based method for rapid calculation of field inhomogeneity due to spatial variation of magnetic susceptibility. Concepts in Magnetic Resonance Part B: Magnetic Resonance Engineering **25B**, 65–78 (4 2005). https://doi.org/10.1002/cmr.b.20034

13. Modat, M., Ridgway, G.R., Taylor, Z.A., Lehmann, M., Barnes, J., Hawkes, D.J., Fox, N.C., Ourselin, S.: Fast free-form deformation using graphics processing units. Computer Methods and Programs in Biomedicine **98**, 278–284 (6 2010). https://doi.org/10.1016/j.cmpb.2009.09.002
14. Oh, G., Bae, H., Ahn, H.S., Park, S.H., Moon, W.J., Ye, J.C.: Unsupervised resolution-agnostic quantitative susceptibility mapping using adaptive instance normalization. Medical Image Analysis **79**, 102477 (7 2022). https://doi.org/10.1016/j.media.2022.102477
15. Salomir, R., de Senneville, B.D., Moonen, C.T.: A fast calculation method for magnetic field inhomogeneity due to an arbitrary distribution of bulk susceptibility. Concepts in Magnetic Resonance **19B**, 26–34 (2003). https://doi.org/10.1002/cmr.b.10083
16. Shmueli, K.: Quantitative Susceptibility Mapping, pp. 819–838 (2020). https://doi.org/10.1016/B978-0-12-817057-1.00033-0
17. Shmueli, K., de Zwart, J.A., van Gelderen, P., Li, T.Q., Dodd, S.J., Duyn, J.H.: Magnetic susceptibility mapping of brain tissue in vivo using mri phase data. Magnetic Resonance in Medicine **62**, 1510–1522 (12 2009). https://doi.org/10.1002/mrm.22135
18. Straub, S., El-Sanosy, E., Emmerich, J., Sandig, F.L., Ladd, M.E., Schlemmer, H.: Quantitative magnetic resonance imaging biomarkers for cortical pathology in multiple sclerosis at 7 t. NMR in Biomedicine **36** (3 2023). https://doi.org/10.1002/nbm.4847
19. Tang, K., Wang, L., Huang, X., Cheng, X., Zhu, Y.M.: Md-sgt: Multi-dilation spherical graph transformer for unsupervised medical image registration. Computerized Medical Imaging and Graphics **108**, 102281 (9 2023). https://doi.org/10.1016/j.compmedimag.2023.102281
20. Vaswani, A., Shazeer, N., Parmar, N., Uszkoreit, J., Jones, L., Gomez, A.N., Kaiser, L.u., Polosukhin, I.: Attention is all you need. In: Guyon, I., Luxburg, U.V., Bengio, S., Wallach, H., Fergus, R., Vishwanathan, S., Garnett, R. (eds.) Advances in Neural Information Processing Systems. vol. 30, pp. 5998–6008. Curran Associates, Inc. (2017), https://proceedings.neurips.cc/paper_files/paper/2017/file/3f5ee243547dee91fbd053c1c4a845aa-Paper.pdf
21. Wei, H., Dibb, R., Zhou, Y., Sun, Y., Xu, J., Wang, N., Liu, C.: Streaking artifact reduction for quantitative susceptibility mapping of sources with large dynamic range. NMR in Biomedicine **28**, 1294–1303 (10 2015). https://doi.org/10.1002/nbm.3383, sTAR-QSM
22. Yao, J., Morrison, M.A., Jakary, A., Avadiappan, S., Chen, Y., Luitjens, J., Glueck, J., Driscoll, T., Geschwind, M.D., Nelson, A.B., Villanueva-Meyer, J.E., Hess, C.P., Lupo, J.M.: Comparison of quantitative susceptibility mapping methods for iron-sensitive susceptibility imaging at 7t: An evaluation in healthy subjects and patients with huntington's disease. NeuroImage **265**, 119788 (1 2023). https://doi.org/10.1016/j.neuroimage.2022.119788
23. Yoon, J., Gong, E., Chatnuntawech, I., Bilgic, B., Lee, J., Jung, W., Ko, J., Jung, H., Setsompop, K., Zaharchuk, G., Kim, E.Y., Pauly, J., Lee, J.: Quantitative susceptibility mapping using deep neural network: Qsmnet. NeuroImage **179**, 199–206 (10 2018). https://doi.org/10.1016/j.neuroimage.2018.06.030
24. Zhao, Y., Qu, H., Wang, W., Liu, J., Pan, Y., Li, Z., Xu, G., Hu, C.: Assessing mild cognitive impairment in parkinson's disease by magnetic resonance quantitative susceptibility mapping combined voxel-wise and radiomic analysis. European Neurology **85**, 280–290 (2022). https://doi.org/10.1159/000522329